WILEY-VCH

DOI: 10.1002/((please add manuscript number))
Article type: Communication

Large range HS-AFM imaging of DNA self-assembly through *in situ* data-driven control

*Adrian P Nievergelt, Christoph Kammer, Charlène Brillard, Eva Kurisinkal, Maartje M.C. Bastings, Alireza Karimi, Georg E. Fantner**

Dr. Adrian P Nievergelt, Charlène Brillard, Prof. Dr. Georg E. Fantner
Laboratory for Bio- and Nano-Instrumentation Ecole Polytechnique Fédérale de Lausanne (EPFL), 1015 Lausanne, Switzerland
E-mail: georg.fantner@epfl.ch
Dr. Christoph Kammer, Dr. Alireza Karimi
Automatic Control Laboratory, Ecole Polytechnique Fédérale de Lausanne (EPFL), 1015 Lausanne, Switzerland
Eva Kurisinkal, Prof. Dr. Maartje M.C. Bastings
Programmable Biomaterials Laboratory, Ecole Polytechnique Fédérale de Lausanne (EPFL), 1015 Lausanne, Switzerland

Keywords: high-speed atomic force microscopy, control system design, resonance compensation, self-assembly, DNA nanotechnology

Abstract

Understanding hierarchical self-assembly of biological structures requires real time measurement of the self-assembly process over a broad range of length- and timescales. The success of high-speed atomic force microscopy (HS-AFM) in imaging small scale molecular interactions has fueled attempts to introduce this method as a routine technique for studying biological and artificial self-assembly processes. Current state of the art HS-AFM scanners achieve their high imaging speed by trading achievable field of view for bandwidth. This limits their suitability when studying larger biological structures. In ambient conditions, large range scanners with lower resonance frequencies offer a solution when combined with first principle model-based schemes. For imaging molecular self-assembly process in fluid however, such traditional control techniques are less suited. In liquid, the time-varying changes in the behavior of the complex system necessitates frequent update of the

compensating controller. Recent developments in data-driven control theory offer a model-free, automatable approach to compensate the complex system behavior and its changes. Here we present a data-driven control design method to extend the imaging speed of a conventional AFM tube scanner by one order of magnitude. This enabled the recording of the self-assembly process of DNA tripods into a hexagonal lattice at multiple length scales.

Main Text

Macromolecular systems with the ability to dynamically assemble and disassemble are ubiquitous throughout technology and nature. Prominent examples are the dynamic self-assembly of microtubules[1] and actin filaments[2,3] in the cytoskeleton of mammalian cells, or networked chemical systems based on nanoparticles[4]. Often, such self-assembly systems exhibit both short-range ordering into a crystal as well as large range effects such as grain boundary formation. In order to understand grain boundary formation and defect healing, one has to observe individual crystal constituents and their interactions close to the boundary. Therefore, a microscope with very high spatiotemporal resolution that is additionally capable of a large field of view is required. Atomic force microscopy (AFM), and in particular high-speed AFM (HS-AFM) has proven to be an invaluable tool to study a wide range of dynamic biological processes[5–8] [9]. However, high-speed scanners generally only have a small displacement,[10,11] and even high-speed scanners designed specifically for a larger field of view are limited in range.[12,13] More traditional scanners such as piezo-tube based designs offer scan ranges of 120µm×120µm or more but suffer from low resonance frequencies which limit the scanning speed severely. When a voltage step is applied to a scanner, the scanners mechanical resonances will be excited, leading to a characteristic ring-down behavior. The dynamics of a liquid meniscus add complex additional resonances to the primary ringing which are difficult to model (**Figure 1a**). When such dynamics are present in a traditional

proportional-integral controller based closed-loop system, as is the case with AFM, increasingly aggressive gains will first amplify the resonances of the system, and finally make the system entirely unstable (**Figure 1b**). Even if the system is still stable, the amplification of the scanner resonances results in ringing artefacts during imaging (**Figure 1c**, lower left) which obscure the real topography (**Figure 1c**, upper right). Previously it has been shown that robust model based control techniques can solve this problem.[14,15] Unfortunately these techniques have not found widespread adoption, since the controller design process involved is extensive (**Figure 1e**) and error prone, requiring the AFM user to have expert knowledge in control system engineering. Especially for experiments that need to be performed in solution, the complex system response, evaporation and capillary motion of the liquid make the dynamic behavior of the scanner highly time-varying (**Figure 1d**), which makes it necessary to frequently redesign the controller. The difficulty in generating good models and the time varying nature of the system makes the implementation of model-based control design techniques impractical. In addition, the result needs to be verified for stability to prevent deployment of an unstable controller. To avoid these issues we propose to apply a novel control design method **Da**ta-driven **R**obus**t** (DaRt) control,[16,17] which is particularly well suited to controlling AFM scanners in liquid. The proposed method requires minimal user interaction, guarantees closed-loop stability[16] and is fully automated (**Figure 1e**, green process), needing only a desired closed-loop bandwidth as input from the user. This automation enables the user to compute a controller and start the experiment within less than a minute. Our approach can compensate almost arbitrary resonances and is therefore suitable for a wide range of different scanners (see **Figure S1**), and allows for fast scanning without compromising scan range. In our implementation, we use the cantilever directly as a sensor to measure the frequency response. This allows to achieve superior controller performance, since the measured response is not only that of the scanner, but of the whole loop including discrete time delays, amplifier dynamics, scanner dynamics and potentially cantilever dynamics.

In order to record high resolution images such as DNA tripod self-assembly, sharp tips are necessary. A common concern in control design for AFM is tip wear or damage due to the identification process. In our implementation, we use a pseudo-random binary sequence (PRBS) as identification signal, which has an optimal Crest factor of 1. In contrast to swept sine as used by a lock-in amplifier, the output signal observed on the cantilever deflection is only minimally perturbed away from its setpoint, indicating that the scanner is not extended significantly during identification. In addition, the nominal amplitudes we use for identification are between 0.5-5nm. In our experiments, we have not observed damage to the tip or the substrate during identification. Thus, we conclude that the tip-sample forces from this type of identification are not large enough to cause damage to the tip. On the contrary, the better control over the feedback-error during scanning reduces tip-sample forces during imaging and helps to preserve the tip.

Figure 2 shows an example of the typical performance that can be achieved with the proposed method. The dynamics of a commercial tube scanner (Bruker AS-12VLR, 12µm range) operated in a liquid environment (**Figure 2a**, green trace) shows a multitude of resonances. The designed controller **(Figure 2a**, red trace) is the result of the automated optimization with the objective of having the closed-loop response of the identified system to behave like a 20 kHz 2^{nd} -order Butterworth low-pass filter (See SI section 2 for details on the formulation and optimization). This control design is based purely on the measured frequency response of the system, and does not require a parametric model. When implemented in the AFM (see **Figure S2**, **Figure S3**, **Figure S4**), the measured closed-loop response (**Figure 2b**, purple trace) is almost identical to the theoretical response that is predicted by the optimization routine (**Figure 2b**, blue trace). A step applied to the deflection signal visualizes the much-improved positioning speed (**Figure 2c**) and recovery of the set-point (**Figure 2d**) when using DaRt control compared to traditional proportional-integral (PI) control. To demonstrate the improved performance, we have imaged plasmid DNA in buffer solution (**Figure 2e**, see SI

section 7 for full images) at increasing scan rates. By using our previously developed high-speed head[18,19] in photothermal off-resonance tapping (PORT) [20] with commercially available high-speed cantilevers (Olympus BLAC-10DS), we ensure a high enough measurement bandwidth to capture all relevant dynamics of the system (200 kHz sampling rate, 195 lines/s limit for one measurement per pixel at 512 px). Even at a relatively low scan speed of 20 lines/s the image taken with the new controller (top right half) appears sharper than with a pure PI controller (lower left half). When increasing the scan speed, using the PI controller quickly results in a blurred image, while DaRt control preserves sharp edges up to 100 lines/s. When increasing the speed further, the improved controller likewise starts blurring the DNA, however the pure PI controller cannot track features at all anymore (~one order of magnitude better tracking at 10kHz, see **Figure S4Error! Reference source not found.a**). Finally, DaRt control cannot only be used for real-time compensation of resonance in *z*-direction, but can also be applied to correcting lateral resonances (see SI, section 6).

We utilized the capabilities of our new technique to resolve the self-assembly dynamics of hexagonal lattices formed using DNA nanotechnology. Planar tripods with blunt ends are formed from three distinct strands.[21] While the blunt ends weakly interact with each other[22], the tripods do not form lattices in solution, even when annealed.[21] When weakly adsorbed to a surface however, the reduction in degrees of freedom increases the effective dissociation constant and leads to the formation of nominally hexagonal 2D crystals. Together, these properties make the blunt-end assembly of DNA an excellent example of a highly dynamic, surface enhanced process with short range as well as long range ordering. Using a conventional tube scanner and the DaRt controller, we can observe the formation of DNA patterns at multiple length scales (**Figure 3a**, full images in **Figure S7**). We have acquired time-lapse recordings of nucleation and formation of hexagonal lattices (**Figure 3b**, Supplementary Video 1). While the 2D crystals form nominally hexagonal patterns, we

observe a significant number of pentagonal and heptagonal structures, especially in the early stages of nucleation and growth. In our observations, these species are less stable than hexagons and growth seems to occur preferably in hexagonal patterns. In order to quantify defect density and location, we have used computer-vision based segmentation and classification on the time-lapse dataset (details in methods section). Using the large range of our scanner, we can analyze the crystallization process over a wide range of different fields of view (**Figure 3c**). The result of the automated segmentation and classification is overlaid on the images (top right half). We find that a heptagonal defect is often accompanied by two pentagonal ones (**Figure 3d**). We hypothesize that this is necessary to minimize the lattice energy in the presence of defects. **Figure 3e** shows the surface density of all three polygonal species over time. Notably, the combined density of defects is initially larger than the density of hexagons. This is likely due to the high flexibility of the DNA tripods which makes pentagonal and heptagonal assemblies likely as long as there is no lattice to stabilize the hexagonal symmetry. Indeed, after the initial nucleation, the defect density seems to saturate while the growth of hexagonal patches is observed to continue at near constant rate. Notably the steady state density of pentagonal to heptagonal defects is close to 2:1, which has been suggested as the energetically lowest defect structure for graphene.[23]

The recording of the self-assembly of DNA tiles into a planar crystal on a variety of different size scales demonstrates the capabilities of our method to increase the scanning speed of most AFM scanners by an order of magnitude while fully preserving the lateral range of the scanner, even when measuring in liquid environment. Additionally, the process provides an optimal, but user-adjustable, I-gain which generally yields the best possible results for the system. This eliminates a difficulty which usually requires the skill of the microscope operator. We have shown here that the data acquired is of high enough quality for automated segmentation and classification and therefore provides an excellent starting point for studying phenomena of forming 2D crystals, such as grain boundary formation, defect formation and

healing, or lattice strain. Finally, the technique can enable the measurement of surface kinetics and surface diffusion of macromolecular self-assembly systems.

Experimental Section

AFM Imaging: Images have been acquired on a home-built small cantilever AFM with photothermal excitation as described elsewhere.[9,19,24] All images in the paper were acquired using photothermal off-resonance tapping (PORT) at frequencies between 120kHz (DNA assembly) and 200kHz (Plasmid scanning) using AC10DS cantilevers (Olympus) with electron-beam deposited carbon tips.[9]

A custom-made silicon O-ring was placed onto freshly cleaved mica and was half-filled by 5mM degassed $MgAc_2$ (diluted from 100mM filtered $MgAc_2$ solution with ultra-pure water). The cantilever was approached to the surface and the surface was scanned to check for contaminations. After the identification and controller design process was performed, the cantilever was retracted from the surface by 1 um and 10uL of the DNA tripod solution was injected close to the cantilever in the dedicated channel of the cantilever holder. The sample was then scanned at a line rate of 60Hz (1024 x 512 px), with I-gain set to the one provided by the controller design and the setpoint minimized while preserving good tracking.

AFM Image Processing: Time lapse sequences were processed using an in-house developed batch processing extension to Gwyddion. Images were treated, in order, with a 2-pixel conservative de-noising filter, median line mismatch corrected, pre-flattened (Flatten Base operation) and finally polynomially line-by-line corrected with an Otsu's mask. Images were then exported in PNG format and assembled into a movie using FFMPEG.

Still images were manually flattened using a combination of plane flattening and masked line matching steps. Small scars were removed by masking where applicable for better visibility.

Segmentation and classification of time-lapse data: Exported grayscale images were loaded into a custom analysis script written in Python. Images were blurred with a 9-pixel gaussian

kernel (for 1 μm and 1.5 μm field of view) and thresholded with an Otsu method. The centers of lattice polygons have been found with the SimpleBlobDetector class from the OpenCV library. Image subsets were generated based on the center coordinates and typical lattice polygon size (side length ~26nm). Subsequently, classes for pentagonal, hexagonal and heptagonal lattice elements were generated and asymmetry and rotation were determined by basin hopping optimization,[25] while the template offsets were matched by OpenCVs templateMatching. Classification is then based on the highest match between the template and the image subset among the pentagonal, hexagonal or heptagonal template.

Frequency response measurement: Acquisition of the frequency domain system response was performed by bringing the AFM into feedback with the surface using either contact mode or PORT and then reducing the gains to small enough values to only compensate drift. The height output was modulated with a pseudo-random binary sequence (PRBS) of order 10 to 12 with a nominal amplitude between 0.5-5nm, depending on the noise level of the system and cantilever used. The deflection was synchronously recorded and frequency domain spectra were calculated using the MATLAB *spa* function with a Hann window length of 700.
Control system design: A novel data-driven method for robust control design based on convex optimization is employed.[16] A key feature is that only the frequency response of the plant is required for the design, and no parametric model is required. A fully parametrized fixed-structure transfer function controller of order 10[26] is designed directly in discrete-time. This has the advantage that no controller discretization step is needed, and that the computed parameters can be directly written to the hardware. While a controller order of 10 has been sufficient for all of our systems, the order of the controller is user selectable and can be, limited by our implementation, increased up to 16 if a system with very complex dynamics is to be controlled for. In order to achieve a desired closed-loop bandwidth while guaranteeing robustness, the control performance is specified as a loop-shaping problem in the H_2 sense

with additional H_∞ constraints. A detailed mathematical formulation as well as the implementation of the optimization is given in the SI, section 2.

Controller implementation: The computed controller is deployed directly to the FPGA (PXIe-7975R with NI 5782 I/O-module) by the LabVIEW software module. The filters are implemented as eight serial second order sections (SOS) in transposed form II design, resulting in a maximum controller order of 16. This filter block is applied to the z-positioning output. Finally, the control loop is closed over the process variable with a digital integrator. While the algorithm computes an ideal integral gain to be used, the value can be optionally tuned by the operator. Each section can be individually disabled in real time to reduce computational delays in the feedback. A more exhaustive description of the controller implementation is given in the SI, section 3.

Plasmid DNA preparation: pUC19 plasmid (X911.1) was bought from Carl Roth (Switzerland) in lyophilized condition and rehydrated with Buffer A (10mM 4-(2-hydroxyethyl)-1-piperazineethanesulfonic acid (HEPES), pH 7.3) to a concentration of 25µg/mL. To remove small DNA fragments, the sample was purified using analytical size exclusion chromatography in a Superose 6 10/300 column on an ÄKTA Pure system (GE Healthcare), resulting in a final concentration of 7 µg/mL for the main fraction.

The DNA sample for AFM was then prepared by pipetting 20 µL of 20 mM $NiCl_2$ onto freshly cleaved Mica, diluting this drop with 20 µL of Buffer A and finally adding 4uL of the purified DNA solution.[27] The sample was left to incubate for about 5 minutes before imaging.

DNA tripod preparation: ssDNA strands 1 (0.6µM), 2 (0.6µM) and 3 (1.8µM) were annealed in 5mM TRIS (BioRad, Cat. No. 161-0716), 1mM EDTA (abcr, Cat. No. 60-00-4), 10mM $MgAc_2$ (abcr, Cat. No. 16674-78-5) buffer as previously reported.[21] The samples were annealed at 80°C for 5 minutes, 60°C for 10 minutes, cooled at a rate of 1°C/hour from 60°C to 20°C for 40 cycles, held at 20°C for 10 minutes and stored at 4°C. Purification of the

annealed product was conducted by running the sample on a 3% agarose gel and excising the band. The flow through was collected from Freeze 'N Squeeze gel extraction spin columns (Bio-Rad, Cat. No. 732-6165) according to manufacturer's instructions. The flow through was pipetted into VIVASPIN TURBO 4, MWCO 3000 (Sartorius, Ref. VS04T91) and centrifuged for 10 minutes at 4350RCF. The retained solution containing the purified tripods was concentrated in a speed vacuum (IR Micro-Cenvac NB-503CIR) at 5000RPM for 6 hours at 35°C. The concentration of the purified tripods was measured by UV-visible spectroscopy. The purified DNA tripods concentration was adjusted to 2.4μM in 5mM TRIS, 1mM EDTA and 10mM $MgAc_2$ buffer prior to imaging.

ssDNA strand 1:

5'-ACTATGCAACCTGCCTGGCAAGCCTACGATGGACACGGTAACG-3'

ssDNA strand 2:

5'-CGTTACCGTGTGGTTGCATAGT-3'

ssDNA strand 3:

5'-AGGCACCATCGTAGGTTTCTTGCCAGGCACCATCGTAGGTTTCTTGCCAGG

CACCATCGTAGGTTTCTTGCC-3'

Supporting Information
Supporting Information is available from the Wiley Online Library or from the author.

Acknowledgements
The authors would like to thank Niccolò Banterle from UPGON at EPFL for help with DNA size exclusion chromatography. We would also like to acknowledge Moritz Durtschi for initial observations on blunt-end DNA tripods.
This work was funded by the European Union's Seventh Framework Programme FP7/2007-2011 under grant agreement 286146, as well as the European Union's Seventh Framework Programme FP7/2007-2013/ERC grant agreement 307338.

Received: ((will be filled in by the editorial staff))
Revised: ((will be filled in by the editorial staff))
Published online: ((will be filled in by the editorial staff))

References

[1] E. M. Mandelkow, *J. Cell Biol.* **1991**, *114*, 977.
[2] T. Lehto, M. Miaczynska, M. Zerial, D. J. Müller, F. Severin, *FEBS Lett.* **2003**, *551*, 25.
[3] S. H. Lee, R. Dominguez, *Mol. Cells* **2010**, *29*, 311.
[4] B. A. Grzybowski, K. Fitzner, J. Paczesny, S. Granick, *Chem. Soc. Rev.* **2017**, *46*, 5647.
[5] T. Ando, N. Kodera, E. Takai, D. Maruyama, K. Saito, A. Toda, *Proc. Natl. Acad. Sci. U. S. A.* **2001**, *98*, 12468.
[6] N. Kodera, D. Yamamoto, R. Ishikawa, T. Ando, *Nature* **2010**, *468*, 72.
[7] J. Preiner, N. Kodera, J. Tang, A. Ebner, M. Brameshuber, D. Blaas, N. Gelbmann, H. J. Gruber, T. Ando, P. Hinterdorfer, *Nat. Commun.* **2014**, *5*, 4394.
[8] N. Chiaruttini, L. Redondo-Morata, A. Colom, F. Humbert, M. Lenz, S. Scheuring, A. Roux, *Cell* **2015**, *163*, 866.
[9] A. P. Nievergelt, N. Banterle, S. H. Andany, P. Gönczy, G. E. Fantner, *Nat. Nanotechnol.* **2018**, *13*, DOI 10.1038/s41565-018-0149-4.
[10] N. Kodera, H. Yamashita, T. Ando, *Rev. Sci. Instrum.* **2005**, *76*, 053708.
[11] T. Fukuma, Y. Okazaki, N. Kodera, T. Uchihashi, T. Ando, *Appl. Phys. Lett.* **2008**, *92*, 243119.
[12] G. E. Fantner, G. Schitter, J. H. Kindt, T. Ivanov, K. Ivanova, R. Patel, N. Holten-Andersen, J. Adams, P. J. Thurner, I. W. Rangelow, P. K. Hansma, *Ultramicroscopy* **2006**, *106*, 881.
[13] H. Watanabe, T. Uchihashi, T. Kobashi, M. Shibata, J. Nishiyama, R. Yasuda, T. Ando, *Rev. Sci. Instrum.* **2013**, *84*, 053702.
[14] G. Schitter, P. Menold, H. F. Knapp, F. Allgöwer, A. Stemmer, F. Allgower, A. Stemmer, *Rev. Sci. Instrum.* **2001**, *72*, 3320.
[15] G. Schitter, R. W. Stark, a Stemmer, *Ultramicroscopy* **2004**, *100*, 253.
[16] A. Karimi, C. Kammer, *Automatica* **2017**, *85*, 227.
[17] C. Kammer, A. P. Nievergelt, G. E. Fantner, A. Karimi, in *Proc. 20th Int. Fed. Autom. Control World Congr.*, **2017**, pp. 10437–10442.
[18] J. D. Adams, A. Nievergelt, B. W. Erickson, C. Yang, M. Dukic, G. E. Fantner, *Rev. Sci. Instrum.* **2014**, *85*, 093702.
[19] A. P. Nievergelt, J. D. Adams, P. D. Odermatt, G. E. Fantner, *Beilstein J. Nanotechnol.* **2014**, *5*, 2459.
[20] A. P. Nievergelt, C. Brillard, H. A. Eskandarian, J. D. McKinney, G. E. Fantner, *Int. J. Mol. Sci.* **2018**, *19*, 2984.
[21] Y. He, Y. Chen, H. Liu, A. E. Ribbe, C. Mao, *J. Am. Chem. Soc.* **2005**, *127*, 12202.
[22] C. Maffeo, B. Luan, A. Aksimentiev, *Nucleic Acids Res.* **2012**, *40*, 3812.
[23] I. Zsoldos, *Nanotechnol. Sci. Appl.* **2010**, *3*, 101.
[24] A. P. Nievergelt, S. H. Andany, J. D. Adams, M. T. Hannebelle, G. E. Fantner, in *IEEE Int. Conf. Adv. Intell. Mechatronics*, IEEE, **2017**, pp. 731–736.
[25] D. J. Wales, J. P. K. Doye, *J. Phys. Chem. A* **1997**, *101*, 5111.
[26] K. Zhou, J. Doyle, K. Glover, *Robust and Optimal Control*, Prentice-Hall, Inc, **1996**.
[27] A. Pyne, R. Thompson, C. Leung, D. Roy, B. W. Hoogenboom, *Small* **2014**, *10*, 3257.
[28] J. Lofberg, in *2004 IEEE Int. Conf. Robot. Autom. (IEEE Cat. No.04CH37508)*, IEEE, **n.d.**, pp. 284–289.
[29] A. P. S. Mosek, **2010**.
[30] D. J. Burns, K. Youcef-Toumi, G. E. Fantner, *Nanotechnology* **2011**, *22*, 315701.

[31] G. Schitter, A. Stemmer, *IEEE Trans. Control Syst. Technol.* **2004**, *12*, 449.
[32] A. P. Nievergelt, B. W. Erickson, N. Hosseini, J. D. Adams, G. E. Fantner, *Sci. Rep.* **2015**, *5*, 11987.

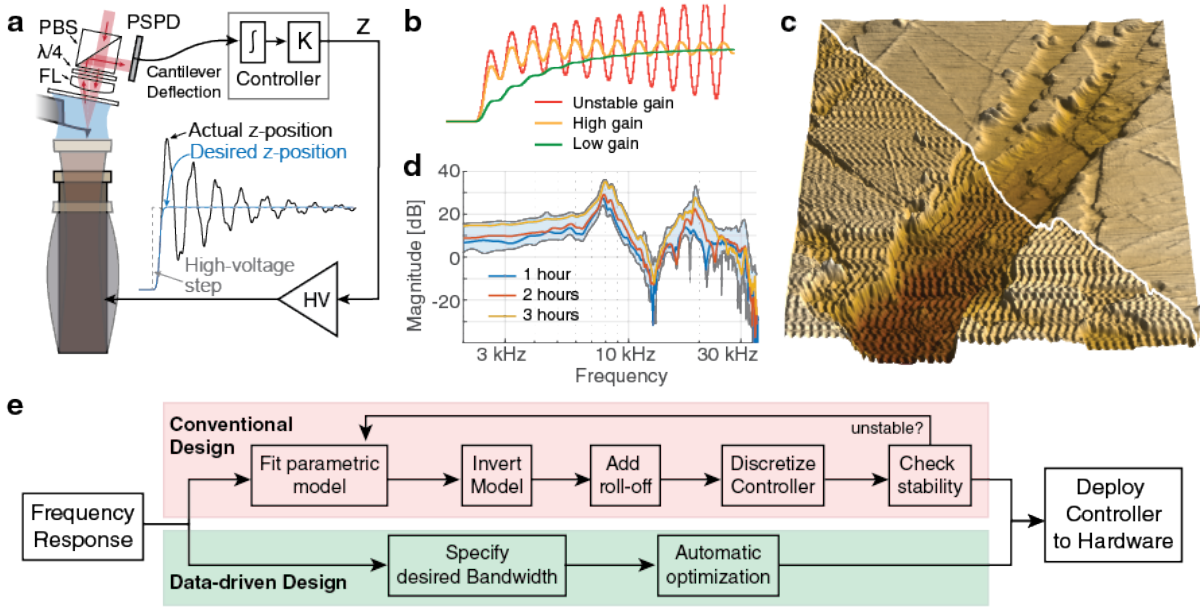

Figure 1. Structural resonances cause instability in AFM feedback, but can be compensated. (a) Schematic of AFM control loop, consisting of the high-voltage amplifier, scanner, cantilever, readout optics, a position sensitive photodiode (PSPD) and the controller, consisting of an integrator and a finite order infinite-impulse response filter K. The scanner acts as a resonator and steps in position introduce complex ringing behavior. (b) In closed-loop operation the ringing of the scanner resonance is amplified by the feedback loop, which for increasingly aggressive gains first introduces visible ringing in the image (green and yellow trace, bottom half of height and error images) and finally leads to complete instability (red trace). (c) When operating in liquid, the dynamic response of the system is highly time-varying due to evaporation and movement of the liquid. Dynamic responses are recorded every 2 minutes. Representative examples are shown at different times into the experiment: 1 hour (blue trace), 2 hours (red trace), 3 hours (yellow trace). The envelope of all recorded traces is shaded as light blue in the background. (d) Setting feedback gains too aggressively amplifies structural resonances which result in strong ripples in the measurement that follow the topography (lower left). When using less aggressive settings, the image resolves clearly without ringing (upper right). (e) Steps required for conventional model-based control requiring active user interaction, extensive knowledge in control system design and significant time to execute. Using data-driven controller design, the process is simplified and the only user input required is the specification of a desired closed-loop feedback bandwidth.

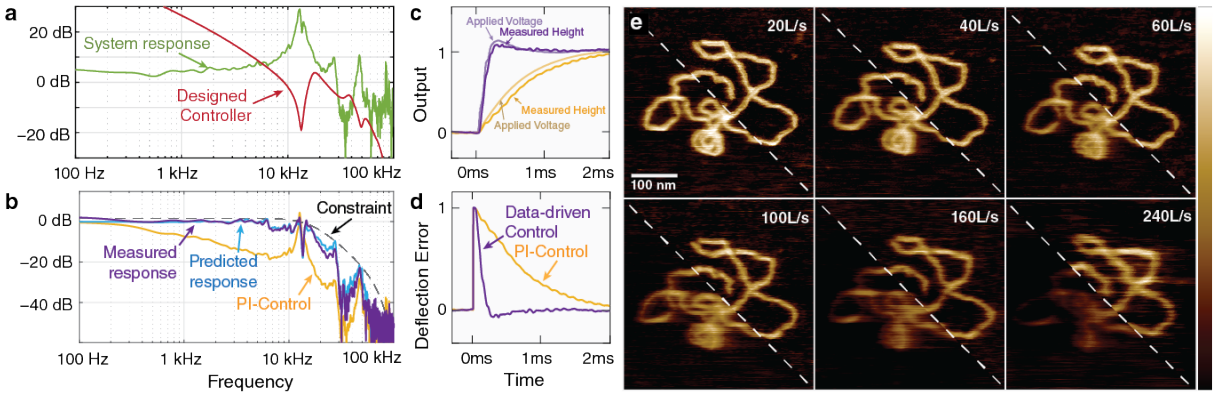

Figure 2. Performance of the proposed control system design method for high-speed scanning. (a) Amplitude response spectra of the microscope in axial direction (green trace) and of the controller designed by DaRt control design (red trace). (b) Predicted (blue trace) and measured closed-loop response of the microscope (purple trace) as well as measured response of a proportional-integral (PI) controller (yellow trace). In contrast to the PI controller, the applied voltage of the DaRt controller contains the complex compensation dynamics which are absent in the measured height by design. The closed-loop response of the data-driven controller is constrained to be below the frequency constraint (dashed black trace). The topography adjustment (c) in response to a deflection error step (d) is significantly faster when using DaRt control (purple traces) than when using traditional PI control (yellow traces). (e) DNA plasmid scanned at increasing line rate in buffer solution. Without filtering (bottom left half), the DNA becomes blurred already at 40 lines/s and completely unrecognizable at 160 lines per second. In contrast, using a feedback with filters (upper right half) preserves the topography well up to high line rates. z-scale is 0-2.5 nm.

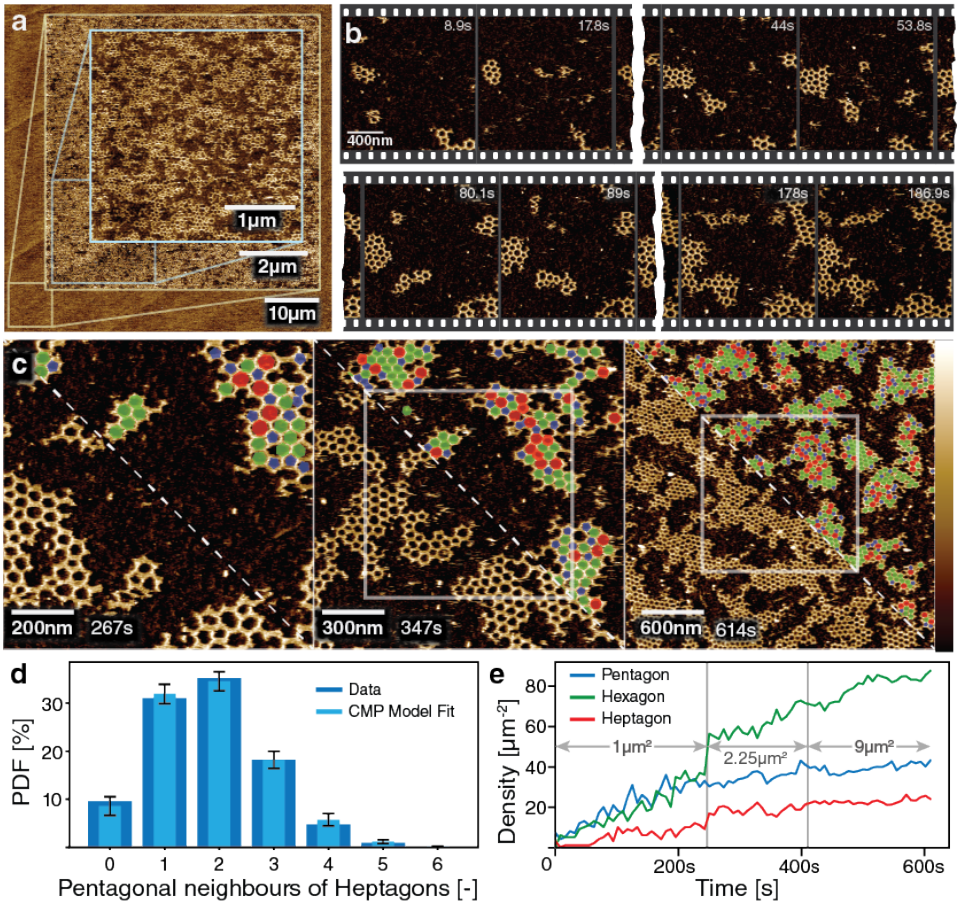

Figure 3. DNA tripod constructs assemble by blunt-end stacking on mica into a mostly hexagonal lattice with pentagonal and heptagonal defects. (a) The scan area of interest can be directly observed and selected from 60µm×60µm to 3µm×3µm. (b) Individual frame grabs of the early nucleation and growth of lattice patches scanned at 60 lines/s. z-scale is 0-3 nm. (c) Consecutive increase of the field of view (last smaller indicated by white rectangle) during the assembly process shows large-scale patch formation. Lattice segmentation and classification into pentagons (blue), hexagons (green) and heptagons (red) is overlayed on the images (top right half). z-scale is 0-3 nm. (d) Number statistic of pentagonal defects next to heptagonal defects, indicating a preferred two pentagonal neighbours per heptagonal defect. The data (dark blue bars) fits well with a Conway-Maxwell-Poisson model (light blue bars, λ=3.71, ν=1.78, error bars are 2σ model uncertainty). (e) Surface densities of pentagons, hexagons and heptagons in the recorded time lapse over different fields of view of the same process. Hexagonal lattice patches continue to grow while defect density saturates with a roughly 2:1 ratio of pentagons to heptagons.

A new control strategy for high-speed atomic force microscopy allows observation of dynamic surface-driven self-assembly over a wide range of size scales. Using minimal user interaction, the method results in a typical increase of an order of magnitude in imaging speed on almost any atomic force microscopy scanner design.

Keyword

*Adrian P Nievergelt, Christoph Kammer, Charlène Brillard, Eva Kurisinkal, Maartje M.C. Bastings, Alireza Karimi, Georg E. Fantner**

Large range HS-AFM imaging of DNA self-assembly through *in situ* data-driven control

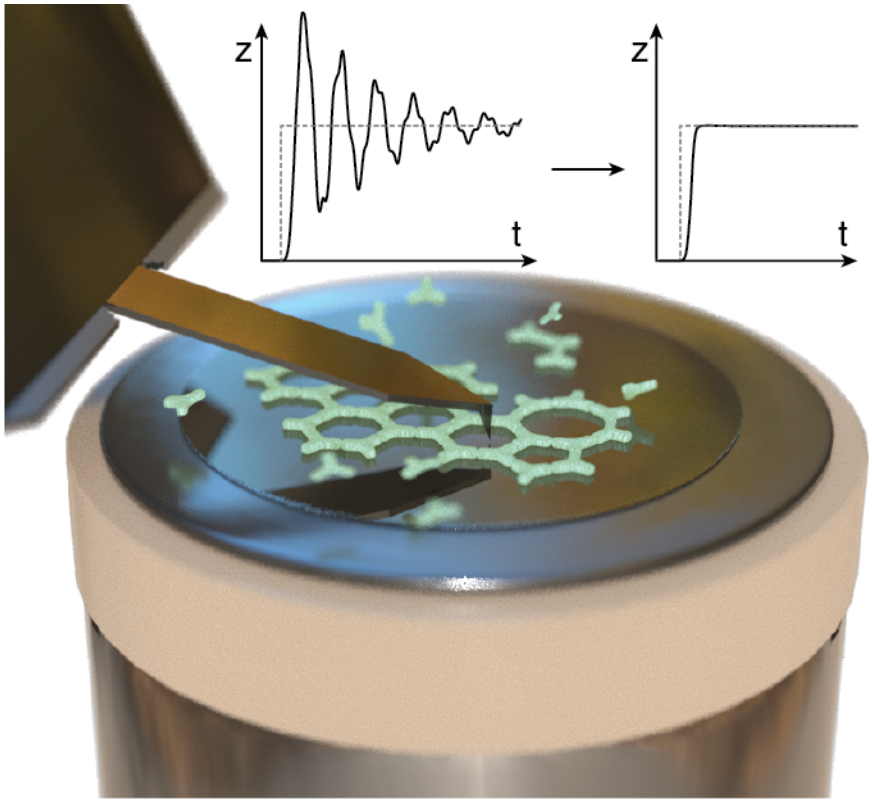

((Supporting Information can be included here using this template))

Supporting Information

Automated resonance compensation for large-range high-speed atomic force microscopy of biomolecular self-assembly in liquid

*Adrian P Nievergelt, Christoph Kammer, Charlène Brillard, Eva Kurisinkal, Maartje M.C. Bastings, Alireza Karimi, Georg E. Fantner**

1. Control system performance on different scanners

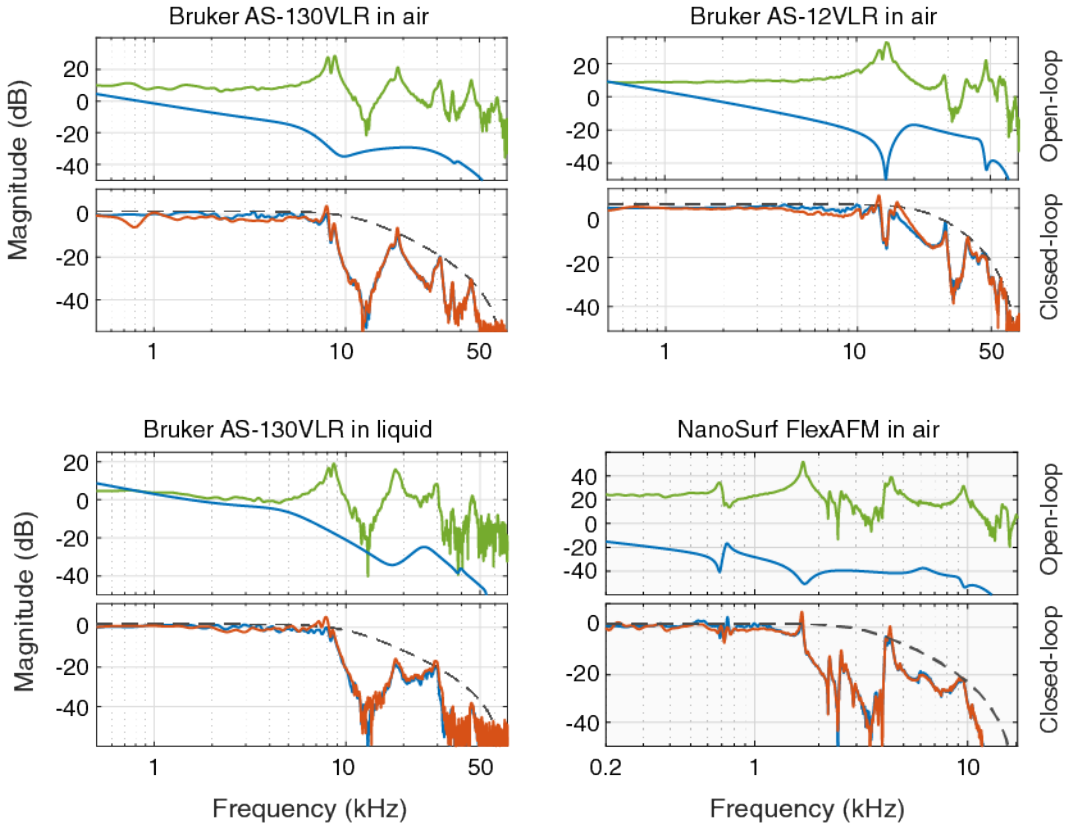

Figure S1: System identification and closed-loop performance on different scanners in air and liquid environment. The top plots show the magnitude plots of the measured frequency response of the plant (green trace) and the response of the computed controller (blue trace). The bottom plots show the magnitude plots of the nominal closed-loop response (blue trace) and the measured closed-loop response (red trace). It can be seen that the nominal and obtained performance match very well. The sensitivity is constrained to be below a Butterworth response (dashed black line). Small violations of this constraint can appear during the design process due to the frequency gridding or due to frequency aliasing in the

measured response. Such small violations do not impact the stability or the positioning performance.

2. Problem formulation and optimization

The control design method requires only the frequency response of the plant for the design, and no parametric model is required:

$$G(j\omega) = G(z = j\omega), \qquad \omega \in \Omega = \{\omega | -\frac{\pi}{T_s} \leq 0 \leq \frac{\pi}{T_s}\}$$

The frequency response can be obtained directly from sample input/output measurement data by using the Fourier analysis method.

The control performance is specified as a loop-shaping problem in the H_2 sense with H_∞ constraints on the closed-loop and input sensitivity. The design is formulated as an optimization problem, where the objective is to design a controller K that minimizes the distance between the open-loop transfer function $L = GK$ and a desired open-loop transfer function L_d:

$$\min_K ||L - L_d||_2, \qquad L_d = \frac{2\pi f_c}{s}$$

where f_c is the desired bandwidth. To guarantee robustness against modeling uncertainty, a constraint on the closed-loop sensitivity $T = GK(1 + GK)^{-1}$ is imposed:

$$||W_2 T||_\infty < 1, \qquad W_2 = (1.2B_w)^{-1}$$

where B_w is a second-order Butterworth lowpass filter with a cutoff frequency of $1.1(2\pi f_c)$. This choice of weighting filter enforces a roll-off of the closed-loop sensitivity above the desired bandwidth, and provide robustness against multiplicative model uncertainty. Further robustness is provided by placing a constraint on the input sensitivity $U = K(1 + GK)^{-1}$:

$$||W_3 U||_\infty < 1, \qquad W_3 = \begin{cases} 10G(j\omega = 0)B_w^{-1} \\ G(j\omega = 0)B_w^{-1} \end{cases}$$

this choice of weighting filter ensures that the controller action is limited in frequencies above the desired bandwidth and provide robustness against frequency-domain model uncertainty. The filter is auto-scaled by the dc-gain of the plant to obtain a general formulation that can be applied to different systems. All performance constraints only depend on the chosen bandwidth f_c and the sampling frequency of the controller, which allows to use the same formulation for a large range of systems without requiring any manual adjustment of the weighting filters.

The controller to be designed is a fully parametrized fixed-structure discrete-time transfer function controller with a fixed integrator:

$$K = XY^{-1} = \frac{x_p z^p + \cdots + x_1 z + x_0}{(z^p + \cdots + y_1 z + y_0)(z - 1)}$$

The method allows to directly design the parameters of the discrete-time controller, and no discretization step is necessary. For implementation, the controller can be separated into an infinite impulse response filter K_F with a dc-gain of 1 and an integral controller:

$$K = K_F(z)\frac{k_i}{(z - 1)}$$

where the gain k_i can be tuned manually by the operator if desired.

The robust control design problem for fixed-structure controllers is non-convex. Previously, we have shown how the problem can be formulated as a convex optimization problem with semi-infinite linear matrix inequality (LMI) constraints.[16] The implementation is then realized by enforcing the constraints on a frequency grid that should well represent the dynamics of the plant.

A frequency grid with $N = 500$ logarithmically-spaced frequency points in the interval $\Omega_N = \left\{0.01\frac{\pi}{T_s}, \frac{\pi}{T_s}\right\}$ rad/s is chosen, where the upper limit is the Nyquist frequency of the controller.

Furthermore, a stabilizing initial controller K_c of the same order as the final controller is required for the design. Since an AFM is always stable by nature, an integral controller with augmented order and low gain is chosen as initial controller:

$$K_c = X_c Y_c^{-1} = (10^{-3} z^p)\left(z^p (z-1)\right)^{-1}$$

Then, the problem can be formulated as a convex optimization problem:

$$\min_{X,Y} \sum_{k=1}^{N} \Gamma_k$$

subject to:

$$\begin{bmatrix} Y^* Y_c + Y_c^* Y - Y_c^* Y_c & (GX - L_d Y)^* \\ GX - L_d Y & \Gamma_k \end{bmatrix} (j\omega_k) > 0 \qquad \text{(Loop Shaping)}$$

$$\begin{bmatrix} P^* P_c + P_c^* P - P_c^* P_c & (W_2 GX)^* \\ W_2 GX & I \end{bmatrix} (j\omega_k) > 0 \qquad \text{(Closed-loop Sensitivity)}$$

$$\begin{bmatrix} P^* P_c + P_c^* P - P_c^* P_c & (W_3 X)^* \\ W_3 X & I \end{bmatrix} (j\omega_k) > 0 \qquad \text{(Input Sensitivity)}$$

$$k = 1, \ldots, N$$

where $\Gamma_k \in \mathbb{C}$ denotes a complex, scalar optimization variable, $P = Y + GX$, $P_c = Y_c + GX_c$, and $(\cdot)^*$denotes the complex-conjugate transpose.

Since the algorithm performs an inner convex approximation of the original non-convex problem around the initial controller, the obtained performance can initially be quite far from the optimal value. The solution is to use an iterative approach, where the computed controller K is used as new initial controller K_c for the next iteration. This choice guarantees closed-loop stability, and the solution converges to a local optimal solution of the original non-convex problem. The iteration can be stopped once the change in the performance criterion is sufficiently small.

This optimization problem is implemented in MATLAB using YALMIP,[28] and solved using MOSEK.[29] To enable a smooth workflow, the control design algorithm can be called directly from LabVIEW, and the time to compute a controller is generally less than a minute.

3. FPGA Implementation

The designed infinite impulse response filter K_F is implemented in hardware using serial second order section (SOS) in transposed form II design, were each section *n* implements the transfer function

$$H_n(z) = \frac{Y_n(z)}{U_n(z)} = \frac{b_{n,0} + b_{n,1} z^{-1} + b_{n,2} z^{-2}}{1 + a_{n,1} z^{-1} + a_{n,2} z^{-2}}$$

Using SOS design significantly improves numerical stability and overflow due to quantization.

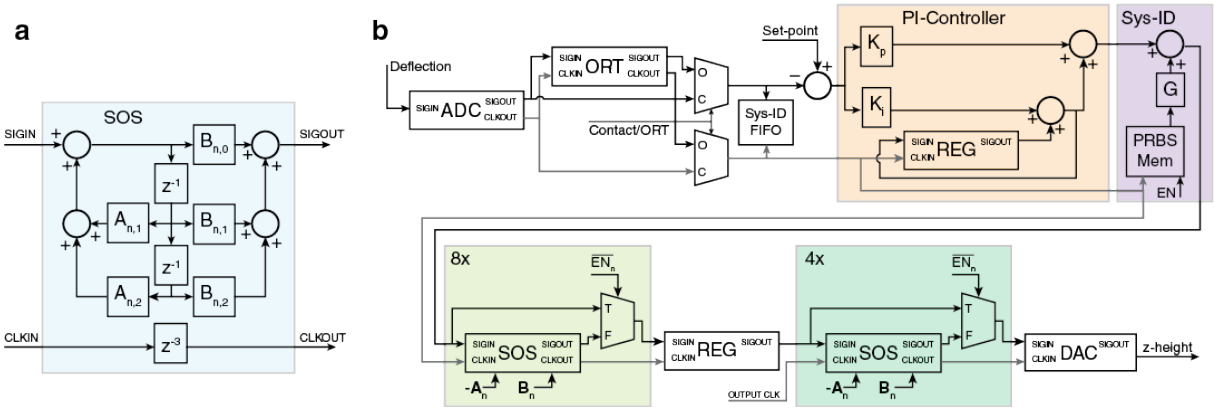

Figure S2: Low-level schematic of the implementation of the filtering blocks and system identification components in the FPGA. (a) Second order section (SOS) functional block with three tick computational delay. Coefficients $A_{n,1\text{-}2}$ and $B_{n,0\text{-}2}$ are implemented in 24-bit fixed-point precision with an 8-bit word length. Signaling between individual SOS blocks is implemented with 26-bit precision and a 9-bit word length. (b) Full flowchart of the control loop. The deflection signal is sampled in an analog-to-digital-converter (ADC) at variable clock rate by decimation. The deflection is either used directly for contact mode AFM or after an off-resonance tapping engine (ORT) as described elsewhere.[9] This process variable is optionally recorded in a direct memory access (DMA) FIFO as well as passed to a PI controller block. After the PI controller, a pseudo-random binary signal (PRBS) modulation can be applied from memory for system identification purposes. This signal then passes through a serial eight SOS blocks resulting in a 16th order filter. The output is buffered in a register (REG) and super-sampled to a higher clock rate for a final serial 4 SOS blocks for signal smoothing before passed to the digital-to-analog converter (DAC).

4. Software interface

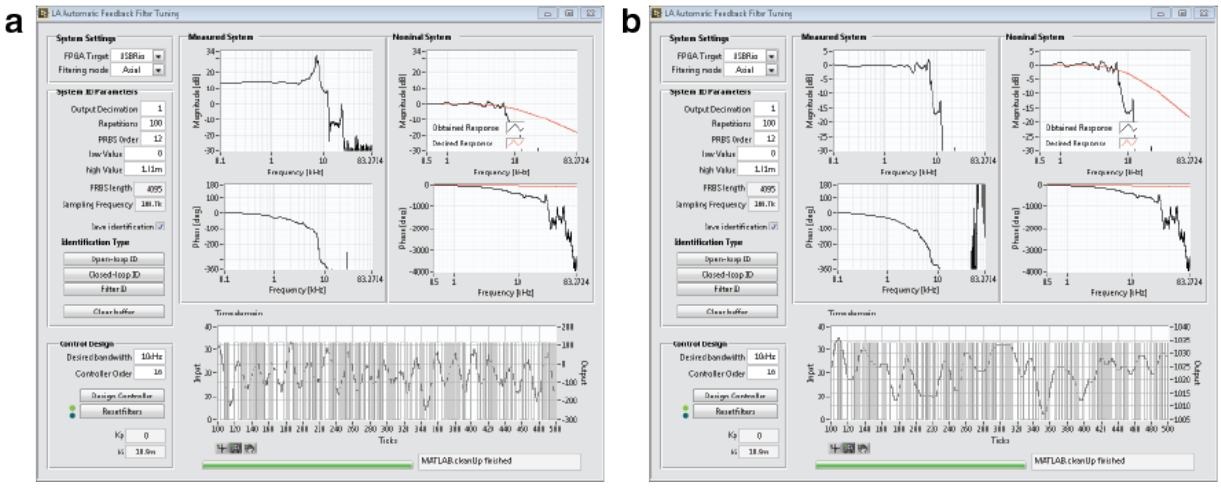

Figure S3: User interface of the automated filter tuning software. (a) Open loop identification of a J-scanner in air (left) with predicted closed-loop response after optimization (right). (b) Closed-loop performance verification. The measured closed-loop response (left) closely matches the previously computed predicted closed-loop response (right).

5. Performance comparison with conventional proportional-integral control

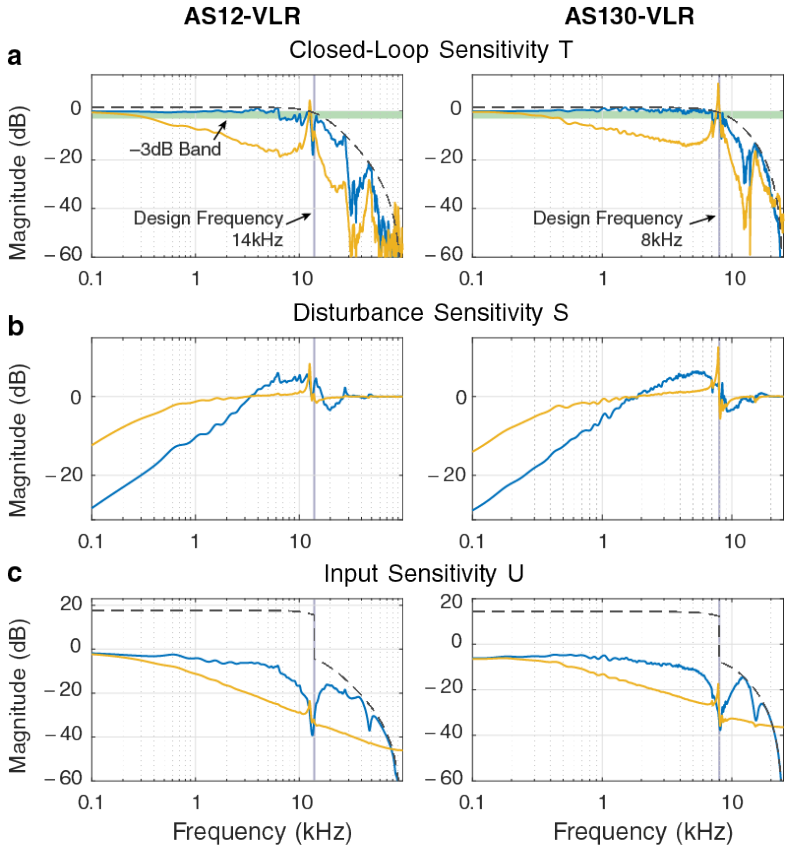

Figure S4: Comparison of closed-loop sensitivities between conventional PI controller (yellow trace) and proposed 10th-order controller (blue trace). The black line indicates the design constraints. (a) The closed-loop sensitivity $T = GK(1 + GK)^{-1}$ shows that the new controller increases the closed-loop bandwidth by one order of magnitude, while also having less overshoot and ringing. (b) The sensitivity $S = (1 + GK)^{-1}$ shows that the new controller provides a significantly better tracking performance and disturbance rejection. (c) From the input sensitivity $U = K(1 + GK)^{-1}$ it can be seen that the new controller does not result in excessive input action.

6. Lateral resonance compensation

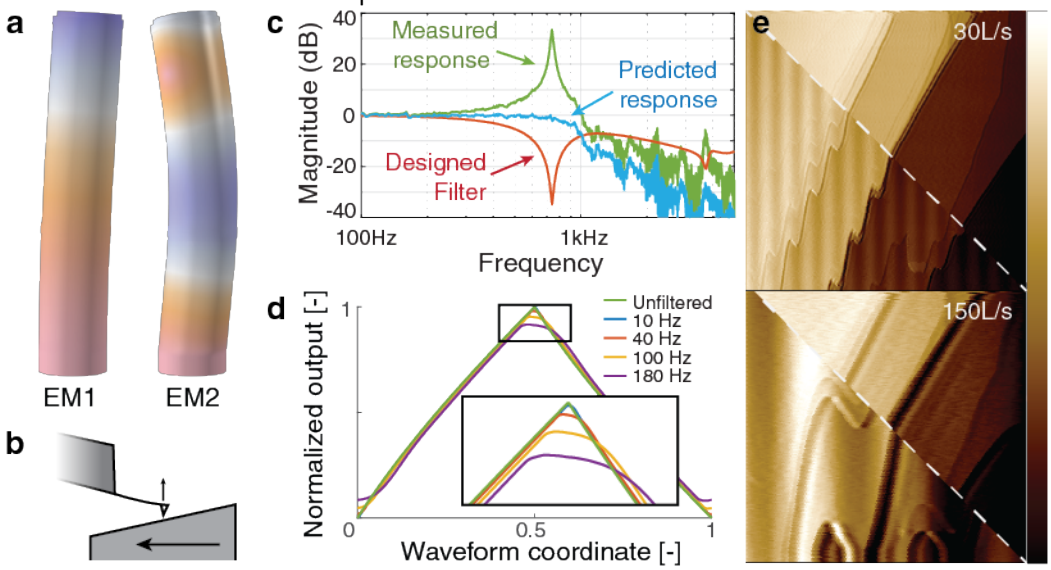

Figure S5: Lateral resonance compensation using data-driven feed-forward compensation. (a) Lateral eigenmodes are excited by the turn-around of triangular scan waveforms. (b) Slope in a sample can be used to detect lateral motion on the deflection of a cantilever. (c) Frequency response of lateral resonances measured using the cantilever in feedback (green trace), the designed filter (red trace) and the predicted combined response (blue trace). (d) Sample fast-axis driving waveforms, output at 10Hz to 180Hz line rate, with and without applied resonance compensation. (e) Comparison of compensated (top right half of images) and uncompensated (bottom left half of images) driving waveforms during imaging of highly oriented pyrolithic graphite. When compensated, the turn-around ripples and the accompanying lateral distortions of the images disappear.

The same data-driven approach can be used to compensate lateral resonances (**Figure S5a**) in addition to the axial resonances. In the presence of slope in the sample, the *x*-*z* coupling can be used to identify lateral resonances directly on the cantilever (**Figure S5b**).[30] Due to the same *x*-*z* coupling, lateral resonances result in characteristic height ripples in addition to spatial distortions in the image (**Figure S5e** bottom left of images).[31,32] Using data-driven control, it is possible to design feed-forward filters that result in a desired frequency domain response of the lateral motion (**Figure S5c**), which can be applied to the triangular scan waveform to compensate resonances in a feed-forward manner (**Figure S5d**). When using compensated drive waveforms, the ripple and image distortions due to lateral resonances can be almost completely eliminated (**Figure S5e**, top right of images).
In the lateral direction, the signal-to-noise ratio of the frequency response depends on the slope of the sample. If the slope is too small, it can be difficult to obtain a good response. One solution to this problem would be to use lateral sensors on the scanner. Since such sensors are already a fixed part of almost all modern AFMs, this would not require additional hardware modifications and could therefore be directly implemented at no extra cost.

7. Full images of plasmid DNA speed comparison

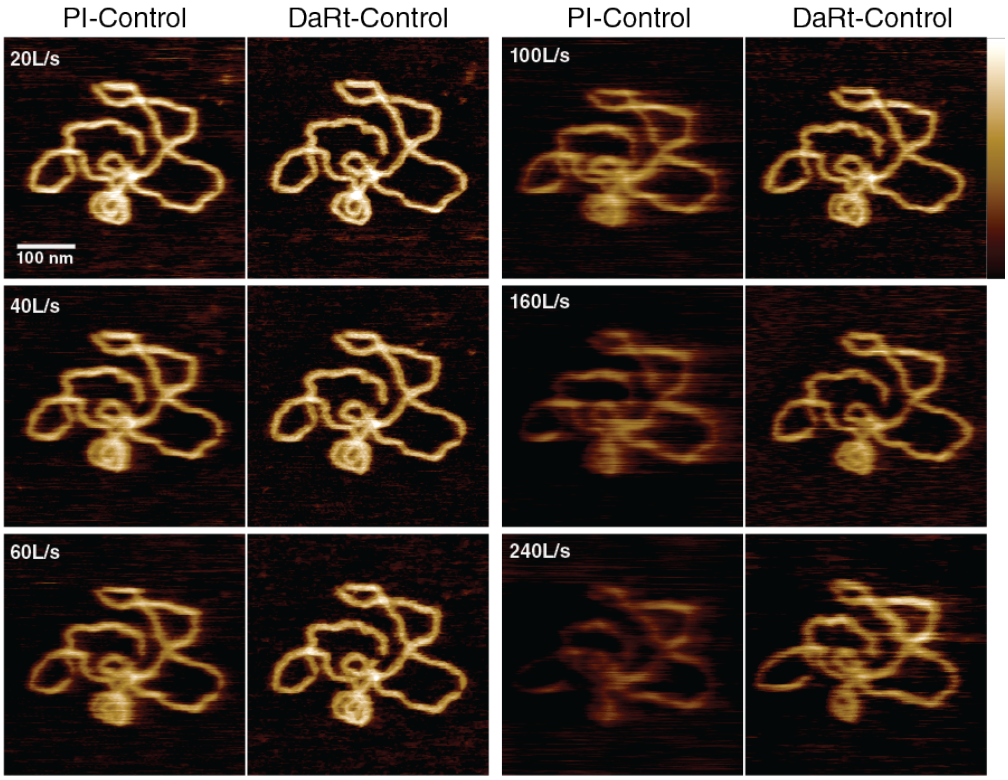

Figure S6: Full images of image quality comparison between DaRt control and traditional PI control when scanning pUC19 plasmid DNA on mica. z-scale is 0-3.5nm

8. Multi-scale imaging of DNA self-assembly

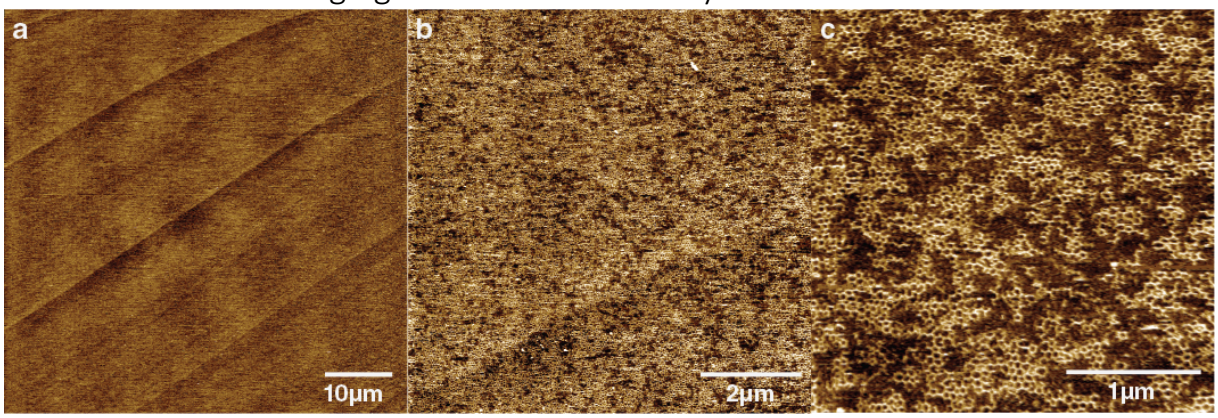

Figure S7: Sequential zoom-ins of DNA self-assembly, with (a) 60µm, (b) 8µm and (c) 3µm field of view.